RSC Advances

PAPER

View Article Online
View Journal | View Issue

Check for updates

Cite this: *RSC Adv.*, 2021, **11**, 24926

Coumarin as a green inhibitor of chloride-induced aluminum corrosion: theoretical calculation and experimental exploration

Huajie Tang,[a] Jianlin Sun, *[a] Daoxin Su,[a] Ying Huang[a] and Ping Wu[ab]

Received 3rd April 2021
Accepted 7th July 2021

DOI: 10.1039/d1ra02622d

rsc.li/rsc-advances

In the present work, the adsorption mechanism and corrosion inhibition effect of coumarin as a green inhibitor was characterized. Quantum chemical calculation and molecular dynamics simulation of the coumarin molecule were performed to get insight into the adsorption model by assessing the frontier orbital parameters and adsorption configuration. The theoretical calculation disclosed that coumarin exhibited a higher adsorption reactivity in the water phase than that in the gas phase, and the C=O structure in coumarin was the most favorable site for adsorption occurring. Coumarin could adsorb spontaneously on an aluminum surface in a parallel manner, where electron donation occurred from the aluminum surface to the inhibitor. Additionally, the experimental investigation determined that coumarin decreased the aluminum dissolution by suppressing both the anodic and cathodic reactions. The optimal coumarin concentration of 0.5 wt% resulted in a maximum inhibition efficiency (89.6%), but coumarin at a higher concentration would lead to the competitive and unstable adsorption of inhibitor molecules, thus decreasing the inhibition effect. Moreover, surface chemical characterization confirmed the formation of Al–coumarin complexes, which was in accordance with the theoretical calculation.

Open Access Article. Published on 16 July 2021. Downloaded on 2/8/2026 1:31:28 PM.
This article is licensed under a Creative Commons Attribution-NonCommercial 3.0 Unported Licence.

1. Introduction

Aluminum strips/foils have received wide attention in industrial and engineering applications, such as machinery, electronics and electrical appliances.[1,2] However, when such aluminum strips/foils are manufactured, serious corrosion-induced pinholes are often formed for the higher electrochemical reactivity of aluminum.[3–5] These defects subsequently reduce the mechanical properties, gas impermeability, electrical and thermal conductivity of aluminum strips/foils. Hence, corrosion inhibitors are commonly employed in cold-rolling operations to reduce corrosion damage of the aluminum surface.

As for the corrosion inhibition of aluminum during cold-rolling operations, most of the commonly used inhibitors are prohibited to avoid residues on the aluminum surface. Herein, some conditions, (I) ash-free, (II) a low boiling point, (III) biodegradable and nontoxic, are established for the selection of potential inhibitors. At present, inorganic and polymer inhibitors are excluded for the limitation of (I) and (II) conditions.[6] Therefore, organic inhibitors are the main focus for the corrosion inhibition of aluminum strips/foils. Coumarin (2*H*-chromen-2-one) consists only of oxygen and carbon, and has been found widely in plants, such as dark bean, chamomile, wild vanilla and orchid, and may be a potential inhibitor. It has been reported that some of the coumarin derivates showed excellent inhibition effects. Mahalakshmi *et al.*[7] studied the synergistic inhibition effect of antibiotics and aminothiazolyl coumarin (3-(2-((4-hydroxybenzylidene)amino)thiazole-4-yl)-2*H*-chromen-2-one, HBATC). The results revealed that HBATC was incorporated into the passive film formation, where the π electrons of the aromatic ring and lone pair of electrons on the heteroatoms contributed to the adsorption reaction between inhibitor molecules and the metal surface. Verma *et al.*[8] synthesized two coumarin derivates, (3-(3-benzyl-4-hydroxy-2-thioxo-3,4-dihydro-2*H*-1,3-thiazin-6-yl)-8-methoxy-2*H*-chromen-2-one, BTMC) and (3-(3-benzyl-4-hydroxy-2 thioxo-3,4-dihydro-2*H*-1,3-thiazin-6-yl)2*H*-chromen-2-one, BTC), and then characterized their inhibition effect through electrochemical experiments, density functional theory (DFT) and a Monte Carlo simulation approach. It has been demonstrated that these derivates could prevent the metal from chloride anion attack by getting adsorbed on the metal surface and the beneficial inhibition effects of the coumarin derivates strongly depended on carbonyl groups and aromatic rings. Although these coumarin derivates with a large molecular weight and high boiling point are resisted in aluminum cold-rolling operations, the above results suggest that coumarin may also protect the aluminum surface from aggressive ions attack. Meanwhile, recent studies have proved that coumarin showed excellent lubrication effects and could be employed successfully in cold-rolling operations.[9,10] Unfortunately, research on corrosion inhibition and

[a]*School of Materials Science and Engineering, University of Science and Technology Beijing, Beijing, 100083, China. E-mail: sjl@ustb.edu.cn; Tel: +86 1062333768*
[b]*Institute of Fundamental and Interdisciplinary Sciences, Beijing Union University, Beijing, 100010, China*

© 2021 The Author(s). Published by the Royal Society of Chemistry

Open Access Article. Published on 16 July 2021. Downloaded on 2/8/2026 1:31:28 PM.
This article is licensed under a Creative Commons Attribution-NonCommercial 3.0 Unported Licence.

surface adsorption mechanism of coumarin, not its derivates, has rarely been reported.

Therefore, the present work aimed to explore the corrosion inhibition effect and adsorption mechanism of coumarin. The chemical reactivity and adsorption properties of coumarin were primarily predicted by quantum chemical calculations and molecular dynamics simulation. The electrochemical behaviours were studied by the dynamic polarization and electrochemical impedance spectroscopy (EIS) measurements. The corroded morphologies were characterized with the scanning electron microscope (SEM). Furthermore, elemental composition and chemical states of the surface were characterized using X-ray photoelectron spectroscopy (XPS) to reveal the adsorption mechanism of coumarin.

2. Experiments

2.1 Theoretical calculation methods

Quantum chemical calculations were carried out using DMol^3 package. The molecular structure was optimized to ensure the true minima on the potential energy surface. Geometrical optimizations were conducted employing the Perdew–Wang (PW91) functions within the generalized gradient approximation (GGA) both in the gas phase and aqueous phase without any symmetry and constraint. The core treatment was set to all electrons with a basis file 3.5. The double-numeric quality plus polarization (DNP) function was performed to all atoms throughout the computation. The solvent effect was considered by employing conductor-like screening model (COSMO) and water was setting as the solvent. The orbital cut-off scheme was set to global with fine quality. The other parameters were set by the inner value of the programs.[11]

According to Koopmans' theory, the electron affinity (A), ionization potential (I), electronegativity (χ), chemical hardness (η), global chemical softness (σ), global electrophilicity index (ω), electron acceptor capability (ω^+) and electron donor capacity (ω^-) are calculated through the following equations:[12–14]

$$\Delta E = E_{\mathrm{LUOMO}} - E_{\mathrm{HOMO}} \quad (1)$$

$$I = -E_{\mathrm{HOMO}} \quad (2)$$

$$A = -E_{\mathrm{LUMO}} \quad (3)$$

$$\chi = \frac{1}{2}(I + A) \quad (4)$$

$$\eta = \frac{1}{2}(I - A) \quad (5)$$

$$\sigma = \frac{1}{\eta} \quad (6)$$

$$\omega = \frac{\mu^2}{2\eta} \quad (7)$$

$$\omega^+ = \frac{(I + 3A)^2}{16(I - A)} \quad (8)$$

$$\omega^- = \frac{(3I + A)^2}{16(I - A)} \quad (9)$$

Besides, the fraction of electrons transferred from coumarin to the metallic atom (ΔN) was calculated as the following formula:[15]

$$\Delta N = \frac{\chi_{\mathrm{M}} - \chi_{\mathrm{CM}}}{2(\eta_{\mathrm{M}} - \eta_{\mathrm{CM}})} \quad (10)$$

where χ_{M} and η_{M} were the electronegativity and hardness of aluminum, respectively. χ_{CM} and η_{CM} represent the electronegativity and hardness of coumarin, respectively. A theoretical value of $\chi_{\mathrm{M}} = 3.23$ eV and $\eta_{\mathrm{M}} = 0$ eV was employed by concerning $I = A$ for bulk aluminum due to the softer chemical hardness of aluminum atoms.

The total energy change (ΔE_{T}) induced by the electron transfer process was further calculated through the equation:[16]

$$\Delta E_{\mathrm{T}} = -\frac{\eta}{4} \quad (11)$$

For a further detailed analysis of reactivity and adsorption mechanisms, Fukui function was calculated to precisely predict the main adsorption sites. Fukui index was favoured to analytically locate the electron transfer sites of organic on the metal surface, which was associated primarily as the derivative of the electron density $\rho(r)$ with respect to the total number of electrons of the system N, under a constant external, $v(r)$.[17,18] Fukui functions can be defined mathematically according to the following equations:[19,20]

$$f(r) = \frac{\partial^2 E}{\partial v(r)\partial N} = \left[\frac{\partial}{\partial v(r)}\right]_N = \left[\frac{\partial \rho(r)}{\partial N}\right]_v \quad (12)$$

$$f_{\mathrm{k}}^- = q_{\mathrm{k}}(N) - q_{\mathrm{k}}(N-1) \quad (13)$$

$$f_{\mathrm{k}}^+ = q_{\mathrm{k}}(N+1) - q_{\mathrm{k}}(N) \quad (14)$$

$$f_{\mathrm{k}}^0 = q_{\mathrm{k}}(N+1) - q_{\mathrm{k}}(N-1) \quad (15)$$

where $q_{\mathrm{k}}(N-1)$, $q_{\mathrm{k}}(N)$ and $q_{\mathrm{k}}(N+1)$ are Mullikan charges at atom k for $N-1$, N and $N+1$ electron system in a frozen orbital approximation, respectively. The f_{k}^-, f_{k}^+ and f_{k}^0 reflected the ability for the electrophilic attack, nucleophilic attack and radical attack, respectively. Herein, the − and + signs referred to the removal and addition of electrons, respectively.

To explore the interaction of coumarin and aluminum surface, molecular dynamics (MD) simulation was conducted using NVT ensemble at 298 K. The MD simulation was carried out in a simulation box ($28.634 \times 28.634 \times 35$ nm^3) with periodic boundary conditions, which contained an amorphous cell of coumarin and three metal layers. The Al (100) plane was set as the target layer for the coumarin adsorption. The coumarin density in amorphous cell was set as 0.3, 0.7 and 1.2 g cm^{-3}, which corresponded a low, medium and high concentration, respectively. Compass (condensed-phase optimized molecular potentials for atomistic simulation studies) forcefield was

Open Access Article. Published on 16 July 2021. Downloaded on 2/8/2026 1:31:28 PM.
This article is licensed under a Creative Commons Attribution-NonCommercial 3.0 Unported Licence.

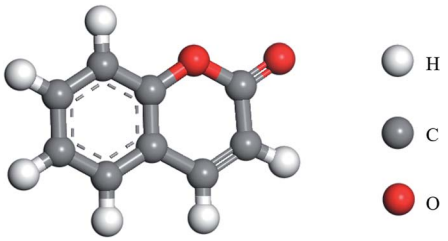

Fig. 1 Molecule structure of coumarin.

Table 1 The physicochemical properties of mineral oil

Properties	Value	Test methods
Kinematic viscosity ($mm^2\ s^{-1}$)	1.60	ASTM D445
Distillation range (°C)	205–235	ASTM D86
Flash point (°C)	80	ASTM D93
Water by distillation	None	ASTM D95
Sulphur content ($mg\ kg^{-1}$)	2	ASTM D129
Colorimetry	30	ASTM D156
Corrosion (grade)	I	ASTM D130

automatically assigned to calculate the dynamic behavior and adsorption energy. The time step was 1.0 fs, and the total simulation time was 1000 ps.

2.2 Materials and preparation

Coumarin with different contents was mixed with 4 wt% lauryl alcohol and balanced mineral oil to model the lubricant in the rolling operations. Moreover, the electrolyte solution was prepared with 0.5 wt% NaCl in deionized water. Coumarin, lauryl alcohol and NaCl were purchased from Shanghai Macklin Biochemical Co. Ltd, China. The mineral oil was consisted of *n*-alkanes, which were obtained from Cangzhou Huahai Refinery Petrochemical Co., Ltd. The structure of coumarin was showed in Fig. 1, and the specific physicochemical properties of mineral oil were listed in Table 1.

2.3 Electrochemical measurements

An autolab PGSTAT302 Potentiostat/Galvanostat system was used in the electrochemical experiments, which contained a conventional three-electrode system with a working electrode, a platinum electrode as the auxiliary electrode and a saturated calomel electrode as the reference electrode. The working electrodes were prepared with pure aluminum (10 mm × 10 mm × 1.5 mm). Prior to the experiments, aluminum specimens were ground sequentially with 2000-, 5000-, and 7000-grit SiC paper and mechanically polished to a mirror-like surface using anti-scuffing paste, followed by degreasing with ethanol, dried at 25 ± 1 °C. The samples were evenly coated with different concentrations of coumarin and then kept in high-pressure reactor at 100 °C for 2 h. The potentiodynamic polarization was scanned from −2.0 V to 1.0 V at 1 mV s^{-1} after a steady open circuit potential (OCP) was reached in the electrolyte solution, and the OCP measurements were conducted for 30 min. The electrochemical impedance spectroscopy (EIS) measurements were performed at the OCP with an AC modulation amplitude of 10 mV in the frequency range of 100 kHz to 0.01 Hz.

2.4 Surface characterization

The surface morphologies were characterized with a laser scanning confocal microscope (LSCM, Olympus, OLS4100, Tokyo, Japan). The microstructure and elemental distributions were analyzed using a scanning electron microscope (FE-SEM, Quanta, FEG 450, Graz, Austria) equipped with an energy dispersive spectroscopy (EDS). Additionally, X-ray photoelectron spectroscopy (XPS, Kratos, Axis Ultra DLD) was applied to investigate the compositions of residues on the aluminum surface. XPS spectra of C, O and Al on the corroded surface were recorded with monochromatic Al Kα radiations (1486.6 eV). The spectra fitting was carried out using PeakFit v4.12 software.

3. Results and discussion

3.1 Reactive properties of coumarin

Quantum chemical calculation by the density functional theory (DFT) was performed in the gas and aqueous (water) phases. Fig. 2 showed the total electrons density (TED) and frontier orbital distribution of the optimized coumarin molecule and its frontier orbital energy. The total electrons density and frontier orbital distributions of coumarin only in the gas phase were displayed for the slight difference of that in the two

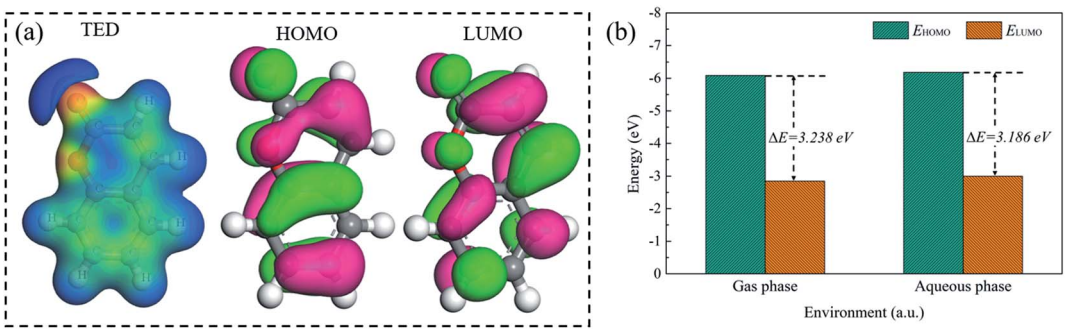

Fig. 2 (a) Total electrons density (TED) and frontier orbital distributions of coumarin in the gas phase, (b) the frontier orbital energy of coumarin.

© 2021 The Author(s). Published by the Royal Society of Chemistry

Open Access Article. Published on 16 July 2021. Downloaded on 2/8/2026 1:31:28 PM.
This article is licensed under a Creative Commons Attribution-NonCommercial 3.0 Unported Licence.

Table 2 Quantum chemical parameters of coumarin

Parameters	Gas phase	Aqueous phase
I (eV)	6.086	6.182
A (eV)	2.848	2.996
χ (eV)	4.467	4.589
η (eV)	1.619	1.593
σ (eV^{-1})	0.618	0.628
ω (eV)	6.616	6.610
ω^+ (eV)	4.131	4.514
ω^- (eV)	8.598	9.103
ΔN	−0.382	−0.427
ΔE_T (eV)	−0.405	−0.398

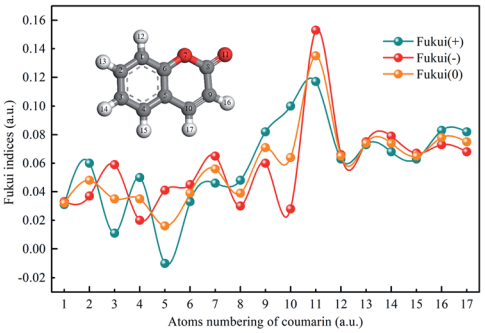

Fig. 3 The variation tendency of Fukui indices with atom numbering of coumarin.

phases. As shown in Fig. 2(a), the reddish area represented a higher density of charge accumulations, while the blue area indicated the charge deficit regions. The reddish areas were mainly around the ester group of coumarin molecule, especially at the O atoms (in C=O structure). This determined that such atoms could provide lone pair electrons to form chemical reactions. Besides, HOMO and LUMO could provide significant information to evaluate the adsorption reactivities of organic molecule. The higher HOMO value indicated a stronger ability to donate electrons, and the lower LUMO value indicated a stronger ability to accept electrons.[21–24] As it can be seen in Fig. 2(b) and (c) that HOMO and LUMO of coumarin spread on the entire molecule structure, revealing that the coumarin molecule could accept both electrophilic attack and nucleophilic attack, while coumarin could adsorb either parallel or obliquely to the metal surface. Meanwhile, coumarin had an energy gap ΔE with a value of 3.238 eV in the gas phase, as shown in Fig. 2(b). It was suggested that the molecule with an energy gap lower than 5 eV may exhibit higher chemical reactivity.[25] Hence, this predicted that the coumarin molecule could be considered as an unstable molecule. In the presence of the aqueous phase, the energy gap of coumarin molecule showed a slight decrease, arriving at 3.186 eV. A lower energy gap was more favoured to the charge transfer. This observation revealed that the water phase could weakly promote the chemical reactivity of coumarin. Additionally, the high value of electron affinity (A), ionization potential (I) and electronegativity (χ) also confirmed that coumarin exhibited a higher reactivity in the aqueous phase than that in the gas phase (Table 2). While the lower value of chemical hardness (η) and higher value of softness (σ) caused a lower charge transfer in the frontier orbital, revealing that coumarin could be easily adsorbed on the metal surface.[26] The increase of electrophilicity index (ω), electron acceptor capability (ω^+) and electron donor capacity (ω^-) indicated that solvent (water) promoted the capability of coumarin molecules to accept and donate electrons. The value of $\Delta N < 0$ indicated electrons donation occurring from metal surface to coumarin molecule.[27] A negative value of ΔE_T also suggested the electrons donation occurring from aluminum surface to coumarin molecule were energetically favourable. The more negative the value of ΔE_T the better the stabilization of the Al–coumarin adsorption film. Hence, a more positive value of ΔE_T in the water phase determined that solvation could promote the adsorption reactivity of coumarin, but it reduced the stability of molecular film.

Table 3 Fukui indices for electrophilic, nucleophilic and radical attacks of coumarin

Atoms	f_k^+	f_k^-	f_k^0	Atoms	f_k^+	f_k^-	f_k^0
C_1	0.031	0.033	0.032	C_{10}	0.100	0.028	0.064
C_2	0.060	0.037	0.048	O_{11}	0.117	0.153	0.135
C_3	0.011	0.059	0.035	H_{12}	0.063	0.066	0.065
C_4	0.050	0.020	0.035	H_{13}	0.073	0.075	0.074
C_5	−0.010	0.041	0.016	H_{14}	0.068	0.079	0.074
C_6	0.033	0.045	0.039	H_{15}	0.063	0.067	0.065
O_7	0.046	0.065	0.056	H_{16}	0.083	0.073	0.078
C_8	0.048	0.030	0.039	H_{17}	0.082	0.068	0.075
C_9	0.082	0.060	0.071				

Fig. 3 showed the changes of Fukui indices with the atoms numbering of coumarin, and the specific values were listed in Table 3. From the calculated Fukui indices, it can be seen that the atoms located around the ester groups (numbered 7–11) showed remarkably higher Fukui indices, of which the O_{11} atom (numbered 11) exhibited the highest Fukui indices. This observation revealed that C=O group was the more favourable site to create adsorption on the metal surface.

The adsorption performance of coumarin with different densities on aluminum surface was simulated. Fig. 4 showed the final configuration of coumarin adsorption on Al (100) surface. Coumarin had a plane structure, therefore, it could attach parallel to the metal surface, covering a larger pure aluminum surface. As shown in Fig. 4(a), at a low density, coumarin showed a low spatial coverage over the metal surface, which could not provide complete protection on the metal surface. However, when coumarin was in a high density, it cannot create a multilayer film, while the excess molecules would induce competitive adsorption, thus decreasing the inhibition effects (Fig. 4(c)). Besides, when coumarin was in the optimal density, the adsorbed molecules effectively could generate a compact film. This effectively reduced the exposed metal surface area and subsequently hindered the metal dissolution at the anode.

© 2021 The Author(s). Published by the Royal Society of Chemistry

Open Access Article. Published on 16 July 2021. Downloaded on 2/8/2026 1:31:28 PM.
This article is licensed under a Creative Commons Attribution-NonCommercial 3.0 Unported Licence.

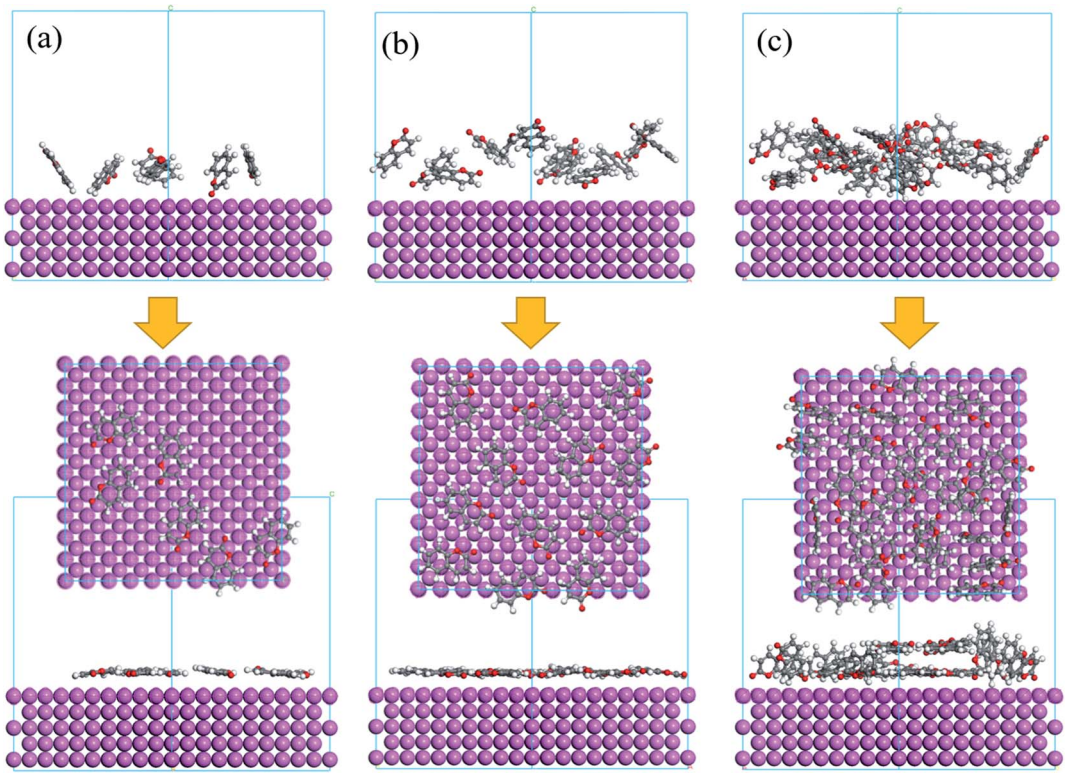

Fig. 4 The final configuration of coumarin adsorption on Al (100) before and after adsorption. (a) Low coverage, (b) optimal coverage, (c) high coverage. Inset is the top view.

3.2 Polarization curves

Fig. 5 showed the potentiodynamic polarization curves of aluminum containing different contents of coumarin. Since some of the curves displayed an incomplete anodic Tafel region, the electrochemical parameters, such as corrosion potential (E_{corr}), corrosion current density (i_{corr}), cathodic Tafel slope (β_c) and corrosion inhibition efficiency (η) were extrapolated from the cathodic branch alone and listed in Table 4. The corrosion inhibition efficiency was defined as:

$$\eta = \frac{i_{corr} - i'_{corr}}{i_{corr}} \quad (16)$$

where i_{corr} and i'_{corr} are corrosion current densities of electrodes without and with different concentrations of coumarin, respectively. As depicted in Fig. 5, the electrode without coumarin (CM-0) displayed the lowest corrosion potential (−0.978 V) and a maximum current density (4.17 μA cm^{-2}), revealing the lowest corrosion resistance of electrode. The CM-0 and CM-0.7 displayed similar electrochemical behaviours, where a higher corrosion potential and a larger corrosion current density occurred. When coumarin content was at 0.5 wt%, the aluminum electrode displayed a minimum current density with a value of 0.43 μA cm^{-2}, which was 89.6% lower than that of CM-0. Herein, it was reasonable to infer that the optimal concentration of coumarin to enhance the aluminum corrosion resistance was 0.5 wt%.

Concretely, the cathodic branches were mainly related to the oxygen reduction at the aluminum/electrolyte interface.

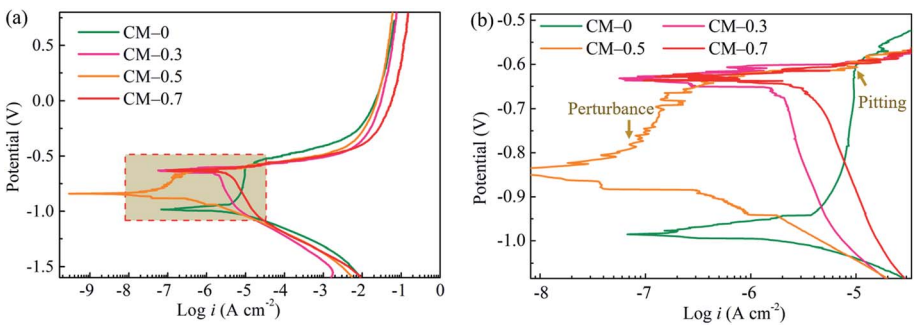

Fig. 5 (a) The potentiodynamic polarization curves for aluminum electrode coated with different contents of coumarin in 0.5 wt% NaCl electrolyte; (b) the magnification of Tafel regions.

© 2021 The Author(s). Published by the Royal Society of Chemistry

Open Access Article. Published on 16 July 2021. Downloaded on 2/8/2026 1:31:28 PM.
This article is licensed under a Creative Commons Attribution-NonCommercial 3.0 Unported Licence.

Table 4 The electrochemical parameters for aluminum electrode coated with different contents of coumarin in 0.5 wt% NaCl electrolyte

Samples	E_{corr} *vs.* SCE (V)	i_{corr} (μA cm^{-2})	β_c (V dec^{-1})	η (%)
CM-0	−0.978	4.17	−0.0147	—
CM-0.3	−0.653	1.41	−0.0148	66.2
CM-0.5	−0.841	0.43	−0.0148	89.6
CM-0.7	−0.636	1.83	−0.0149	56.1

Coumarin displayed a significant inhibition effect on the cathodic reactions, and such beneficial effects were closely related to its concentration. When potential was below about −1.1 V, all cathodic branches remained a similar variation. However, when the applied potential continued to increase, a remarkable discrepancy was encountered for the usage of coumarin. From the magnification in Fig. 5(b), as it can be seen that the cathodic branch of CM-0.5 decreased slowly with a weak fluctuation, but that of CM-0.3 and CM-0.7 decreased sharply.

Furthermore, the anodic branches correlated with the metal dissolution and predominated by the inhibitors, which was accompanied by the pitting and passivation process. The changes of current density were resulted frequently from the protective film formation and their breakdown.[28,29] In the cases of CM-0, the anodic current density showed a clear reduction near the Tafel region, determining the occurrence of protective film. The applied potential approaching the pitting formation potential caused the failure of a protective film and was followed by an abrupt increase of current density. Whereas, the difference was that CM-0.5 showed a fluctuating anodic branch, while its pitting formation potential was rather close to that of CM-0. These current perturbances were generally considered as the proof of protective film rupture and their re-building at the metallic surface, reflecting the nucleation and growth of pitting.[30,31] These transient changes of current density caused the generation of metastable pits at surface,[32–34] thereinto, some of pits would repassivate immediately, but the others would continue to grow and ultimately cause damage to the metallic surface.[35] It was supposed that the instability of this film was concerned with the adsorption of coumarin on the surface. Similar phenomena were commonly observed in the investigation of inhibitors.[33,36,37] Additionally, as it can be seen from the curves of CM-0.3 and CM-0.7 that there were no Tafel slop occurring. In the studies of Lamaka *et al.*,[38] it was pointed out that the pitting formation potential approaching the corrosion potential would break the integrity of the anodic Tafel region. The usage of 0.3 wt% and 0.7 wt% coumarin made corrosion potential increased and approached the pitting formation potential, ultimately, leading to the anodic Tafel slope to be covered. Moreover, the limited ions diffusion also showed remarkably affection on the electrochemical reactions. The ionic migration through the protective film and then would result in the metal dissolution at the electrolyte/aluminum interface. At the terminal segment of polarization curve, coumarin showed little impact on aluminum corrosion and the current density was almost constant with increasing potential.

3.3 Electrochemical impedance spectroscopy

The Nyquist and Bode plots reflected the changes of real impendence and imaginary impendence occurring at the metal/electrolyte interface, as shown in Fig. 6. The single broad semicircle resulted from the two overlapped time constants, which reflected the capacitive characteristic of the aluminum corrosion process. The high frequency (HF) semicircle was attributed to charge transfer resistance and double-layer

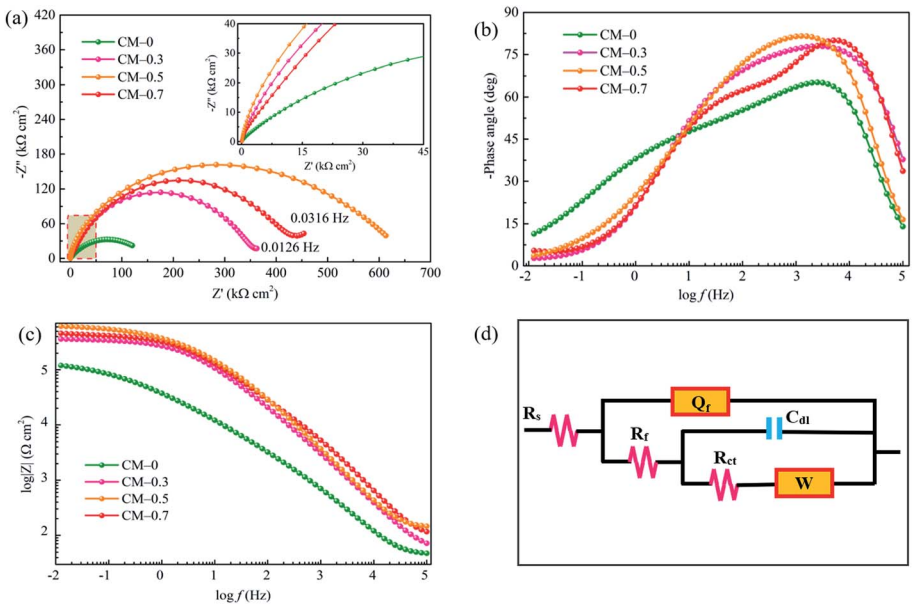

Fig. 6 EIS spectra for aluminum electrode coated with and without coumarin in 0.5 wt% NaCl solution: (a) Nyquist diagrams, (b) phase angle, and (c) impedance modulus; (d) the equivalent circuits used in simulating the electrochemical impedance spectra.

Open Access Article. Published on 16 July 2021. Downloaded on 2/8/2026 1:31:28 PM.
This article is licensed under a Creative Commons Attribution-NonCommercial 3.0 Unported Licence.

capacitance, which closely depended on the chemical composition and surface states of aluminum electrode.[39] The surface roughness and composition inhomogeneities of the aluminum electrode were dominant for such capacitive-loop dispersion from a standard circle. The diameter of the capacitive loop was associated with the interfacial impedance, which peaked at coumarin concentration of 0.5 wt%, then followed by CM-0.7. This determined that coumarin could effectively impair the ions transfer from electrolyte to aluminum surface. When coumarin content was 0.3 wt% and 0.7 wt%, the Nyquist plots showed a straight line after about 0.0126 Hz and 0.0316 Hz, respectively. In general, the low frequency (LF) straight was triggered by the Warburg impendence for the ion's diffusion at the aluminum/electrode interface. The presence of Warburg impedance confirmed that the interfacial charge transfer was strongly retarded by coumarin, and the ions diffusion was going to play a pronounced role in the corrosion process.

Furthermore, Bode spectra revealed the response of phase angle and resistance modulus with the frequency. As can be seen in Fig. 6(b) and (c), there was a linear dependence between $\log|Z|$ *vs.* $\log f$ with a slope nearly close to 1, and the phase angle extended from 0 to 80°. This revealed a typical capacitive behavior and also demonstrated the existence of the CPE exponent. The Bode phase diagram showed the broad phase angle change, spreading from 1 Hz to 100 kHz, which was accounted for the appearance of the two overlapped time constants. The time constants at HF range were motivated by the coating protective layer, which indicated that the coating protective layer possessed a certain thickness. The medium frequency (MF) response was ascribed to the oxide layer of the aluminum surface. Snihirova *et al.*[40] pointed out that the above time constants could model the electrical barrier capacities of the interface. The time constant at the LF presented charge transfer resistance that related to the localized corrosion at metallic/electrolyte interface. The severely localized corrosion occurred when the surface had no effective inhibition effects. The localized corrosion resulted in the formation of the ions transfer channels through the coating and oxide layer, and these channels allowed the electrolyte intrusion and then caused the surface destruction. As seen in Fig. 6(b), all the specimens showed similar changes in the phase angles, but in the absence of coumarin, one of the time constants shifted to the lower frequency. Such observations have resulted from the different surface structures of aluminum when the specimen was prepared without coumarin.

The simulation displayed the detailed interpretation of the EIS spectra, which allowed to decouple the various electrochemical components. The equivalent circuit was depicted in Fig. 6(d). R_s, R_f and R_{ct} represented the resistance of the electrolyte, protective layer (coating and oxide layer) and the double layer, respectively. Considering the surface inhomogeneous/roughness induced frequency dispersion,[41] a constant phase element (CPE) is introduced and give as:

$$Z_{CPE} = \frac{1}{Y_0(\omega j)^n} \quad (17)$$

where Y_0 is the CPE constant; ω is the angular frequency; j is an imaginary number ($j^2 = -1$); and n is dispersion index ranged from 0–1. Q_f and C_{dl} are the capacitances of coating and double layer. Additionally, Warburg resistance was used to model the impendence of ions diffusion. As mentioned above, the electrochemical resistance was remarkably affected by the coumarin concentration, indicating a dominant role of coumarin played in corrosion process.

3.4 Surface topography

Pitting was the main failure mechanism for aluminum. The diameter and depth of holes/pits were dependent on the type of material, corrosive medium and properties of the environment that aluminum was exposed to.[42] Fig. 7 showed the corroded topographies of aluminum electrode, where pitting was dominant. From the 3D morphologies, electrode surface of CM-

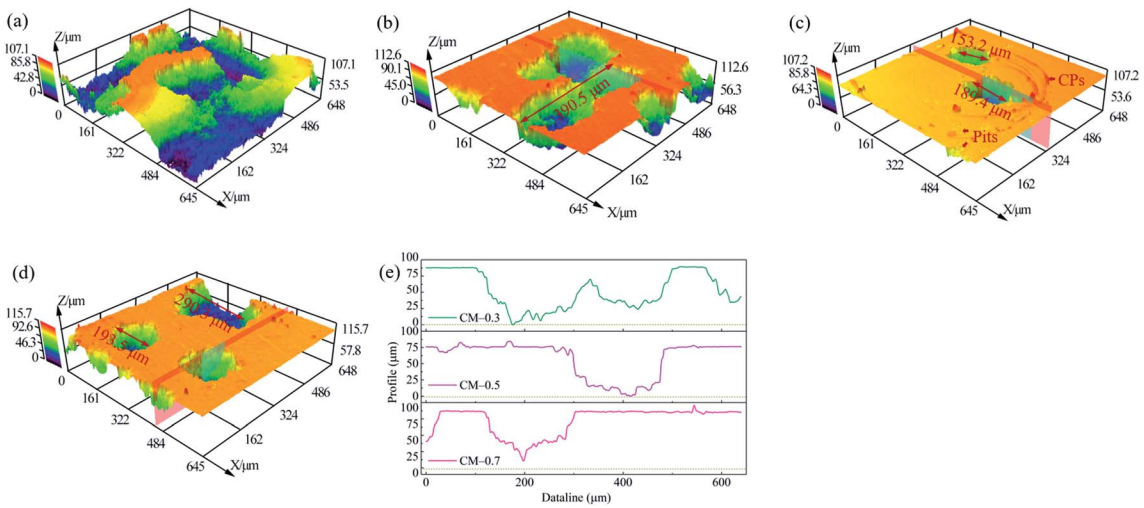

Fig. 7 Surface morphologies of aluminum electrode coated with different contents of coumarin in 0.5 wt% NaCl electrolyte. (a) CM-0, (b) CM-0.3, (c) CM-0.5 and (d) CM-0.7; (e) the cross-sectional profiles of aluminum electrode in (b)–(d).

© 2021 The Author(s). Published by the Royal Society of Chemistry

Open Access Article. Published on 16 July 2021. Downloaded on 2/8/2026 1:31:28 PM.
This article is licensed under a Creative Commons Attribution-NonCommercial 3.0 Unported Licence.

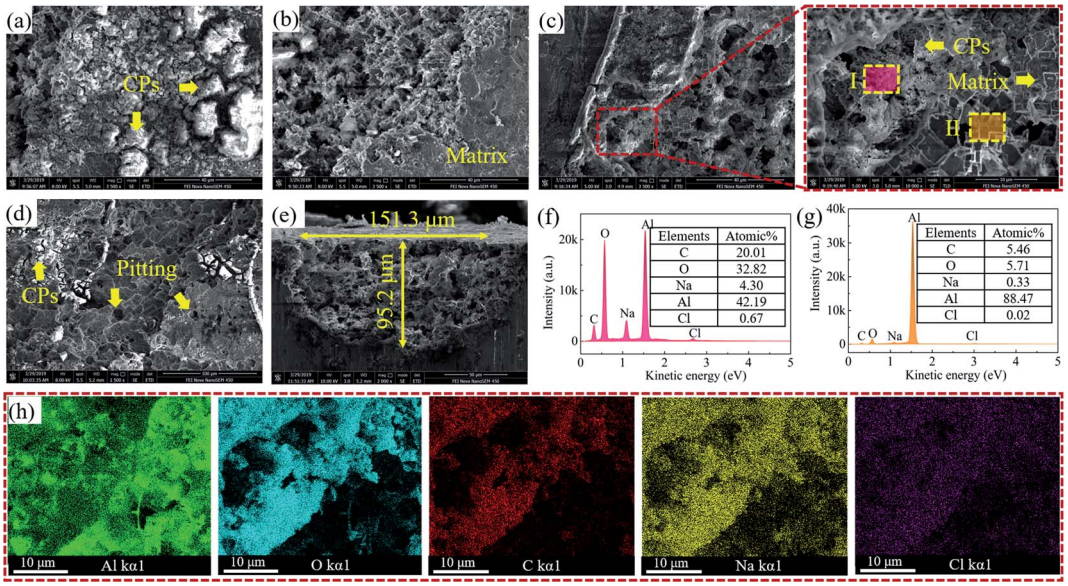

Fig. 8 SEM images of aluminum electrode coated with different contents of coumarin. (a) CM-0, (b) CM-0.3, (c) CM-0.5, (d) CM-0.7; (e) cross-sectional pattern of pits; (f–h) the corresponding EDS results.

0 suffered the most severe corrosion, where pitting adequately developed and caused serious damage. However, when coumarin was applied, corrosion was significantly impaired, accompanying by the remarkable decrease in density and size of pits. Lots of pinholes occurred at the CM-0.3 and the maximum length of that was around 390.5 μm. When coumarin concentration reached 0.5 wt%, corrosion resistance of aluminum was effectively improved, thus inhibiting the nucleation and growth of pitting. The diameters of pits were about 153.2 μm and 189.4 μm, which were lower than that of others. Besides, there were also numerous corrosion products (CPs) and minor-scale pits distributed at the surface. As mentioned in polarization curves, these pits were closely related to the pitting nucleation. In the like manner, the larger size of pits also observed at CM-0.7 electrode surface, revealing a decrease in corrosion resistance with the increase of coumarin concentration from 0.5 wt% to 0.7 wt%. Additionally, Fig. 7(e) showed the cross-sectional profiles of pit in Fig. 7(b)–(d). All pits showed an approximate symmetric shape and their bottom displayed cone shape, suggesting that pitting nucleation and then developed perpendicular to the surface.

3.5 Surface elements and chemical states

Fig. 8 showed the corroded surface of aluminum coated with different contents of coumarin in chloride-containing environment. When there was no coumarin applied (Fig. 8(a)), the electrode was corroded severely and lots of corrosion products with loose structure appeared. The redeposited corrosion products acted as the cathode and provided favourable sites for oxygen reduction. Their specific structures allowed the passing of aggressive ions to the matrix, thus promoting the metal dissolution.[43,44] When coumarin was applied, the fraction of uncorroded surface improved, determining the great inhibition effect of coumarin. The corroded aluminum showed a porous structure due to the aggressive ions attack. From the elemental characterization of corrosion products (area I) and corroded aluminum (area II), the EDS results showed that the fraction of C, O and Cl elements in corrosion products was evidently higher than that in matrix. This suggested that corrosion products mainly comprised aluminum oxides/hydroxides and carbon compounds, whereas the aluminum matrix only included small amounts of carbon compounds. Such carbon compounds were closely related to coumarin and other organic compounds. The EDS maps further determined that corrosion products contained more C, O and Cl than corroded aluminum. The high concentration of Cl in corrosion products confirmed the hypothesis that the loose structure of corrosion products favoured the adsorption and penetration of aggressive ions and thus accelerated the electrochemical corrosion of aluminum.

In order to further identify the elemental compositions and chemical states of corroded surface, the XPS characterization on CM-0.5 aluminum surface was conducted, and Fig. 9 showed the deconvoluted XPS spectra and the wide spectra. The binding energies were corrected for charge effects by referencing the C 1s peak at 284.8 eV.[44] The C 1s spectra were deconvoluted into four characteristic peaks. Thereinto, the peak at 284.8 eV was attributed to the C–C bonds, which was mainly related to the alkanes and dodecyl alcohol; the peak at binding energy of 285.7 eV was assigned to the C–OH structure in both dodecyl alcohol and coumarin; The peak at binding energy of 284.2 eV was relevant to the C=C structure in coumarin; and the peak at a binding energy of 289.2 eV was originated from C=O group in coumarin molecule. In particular, the peak of C=O group showed a slight negative shift from 289.7 eV to 289.2 eV, determining the presence of adsorption-induced charge effects between coumarin and aluminum surface. In the studies of Abdel-Gaber *et al.*,[45] it was revealed that the chemisorption

Open Access Article. Published on 16 July 2021. Downloaded on 2/8/2026 1:31:28 PM.
This article is licensed under a Creative Commons Attribution-NonCommercial 3.0 Unported Licence.

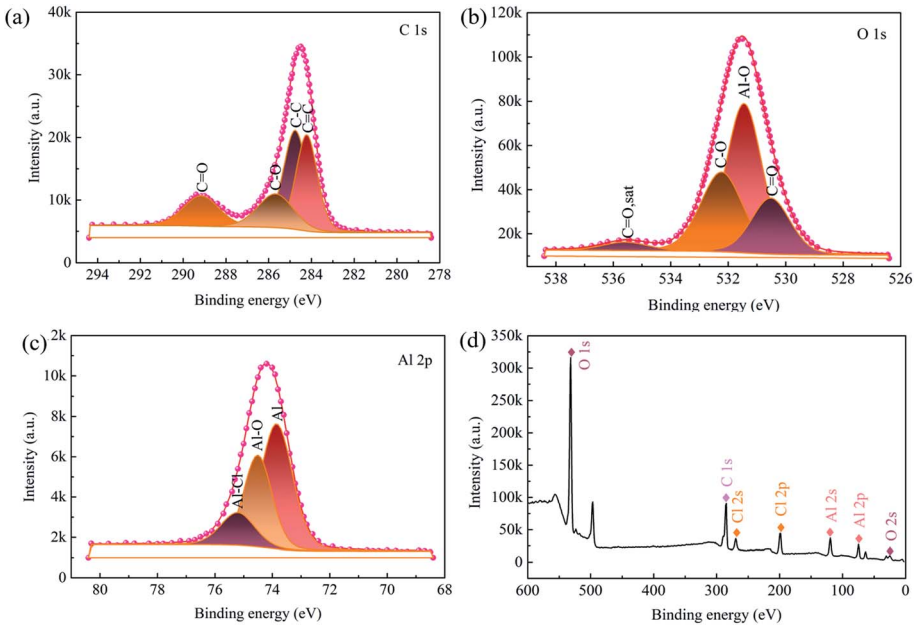

Fig. 9 XPS spectra of aluminum surface of CM-0.5. (a) C 1s, (b) O 1s, (c) Al 2p and (d) wide spectra.

involved charge transfer between the functional groups in molecules and the metallic surface, and then caused a coordinate bond to be formed. Hence, it was confirmed that the surficial film comprised Al–coumarin complexes. This agreed well with the investigations conducted by Xhanari *et al.*[42] Moreover, the corresponding O 1s spectra were observed at the binding energy of 530.6 eV. The core-level spectra of aromatic and unsaturated structures were frequently coupled with a shake-up peak on the high binding energy side of the main photoelectron peak. Herein, the weak peak at 535.6 eV was ascribed to the satellite peak of C=O structure, which well proved the presence of coumarin on the aluminum surface.[10] The peak at 531.4 eV showed the strongest intensity, which conformed to aluminum oxides/hydroxides, *i.e.*, Al_2O_3 and $Al(OH)_3$. This revealed that the chemical composition of the corroded surface was predominated by Al_2O_3 and $Al(OH)_3$. Since the C–O structure existed both in the dodecyl alcohol and coumarin, herein, the peaks of C–O structure at 532.6 eV showed a higher intensity than that of C=O structure. Moreover, there were three deconvoluted peaks for Al 2p spectra. The binding energy of the peak at 74.0 eV was assigned to Al matrix, while the characteristic peaks at 74.6 eV and 75.5 eV were attributed to aluminum oxides/hydroxides and $AlCl_3$, respectively.[46,47] Among them, Al matrix showed the strongest intensity, followed by the Al_2O_3, and $AlCl_3$ with the lowest intensity.

4. Discussion

Coumarin was an effective inhibitor to the corrosion-induced pinholes on aluminum surface, and its effective inhibition was attributed to the Al–coumarin adsorption film (Al–CM film) at the aluminum/electrolyte interface.[48] Surface characterization has determined that both the Al_2O_3 and Al–CM film existed on the aluminum surface. Herein, aluminum corrosion was strongly related to the surface-oxidation/coumarin-adsorption and their further destruction. In the studies of Garrigues *et al.*,[49] it was suggested that the coverage of inhibitors on surface could restrain the adsorption of chloride ions and the destruction of oxide layer on the aluminum surface. Such adsorption film and oxide film could together improve the interfacial impedance of aluminum/electrolyte. Fig. 10 showed the schematic diagrams of corrosion inhibition mechanism of coumarin on the aluminum surface. When coumarin was employed, both Al–CM film and Al_2O_3 were established, this bilayer structure could provide more dense shielding effects for ions attack. As experimentally results showed, the adsorbed coumarin suppressed both the cathodic hydrogen evolution and anodic metal dissolution. Wang *et al.*[3] also confirmed the findings and suggested that the coverage of organic molecules on aluminum surface restrained the hydrogen evolution, thus impeding the cathodic current density. There were two possible cathodic reactions, one was the reduction of water, given as follows:[50,51]

$$2H_2O + 2e^- \rightarrow H_2 + 2OH^- \quad (18)$$

the other was the reduction of dissolved oxygen in water, represented by:[52]

$$O_2 + 2H_2O + 4e^- \rightarrow 4OH^- \quad (19)$$

This adsorbed coumarin film was not conducive to oxygen adsorption or hydrogen evolution, thus restraining the cathodic reactions. Besides, in the cases of the anodic dissolution, the bilayer structure reduced the contact between the metal matrix and the aggressive ions, thus impaired the following reactions:

© 2021 The Author(s). Published by the Royal Society of Chemistry

Open Access Article. Published on 16 July 2021. Downloaded on 2/8/2026 1:31:28 PM.
This article is licensed under a Creative Commons Attribution-NonCommercial 3.0 Unported Licence.

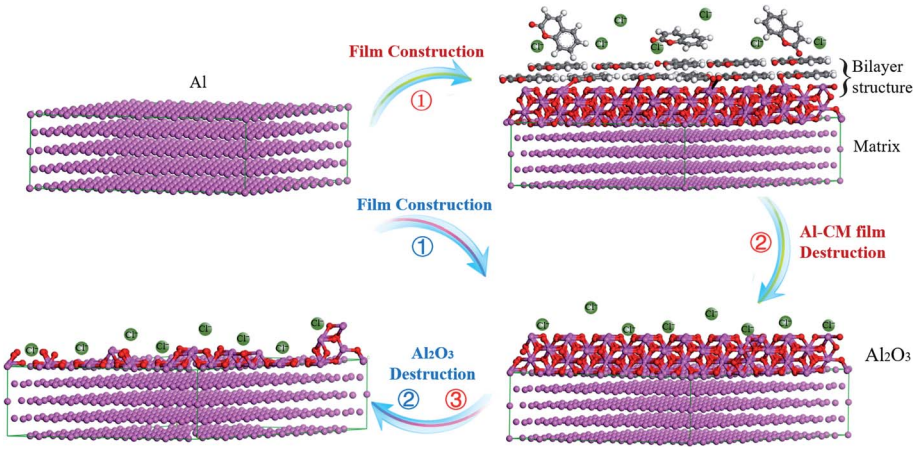

Fig. 10 Schematic diagrams of the corrosion inhibition mechanism of coumarin in chloride-containing environment.

$$Al \rightarrow Al^{3+} + 3e^{-} \quad (20)$$

However, the continuous chloride attack would result in the CM-film construction and Al_2O_3 exposure. Then, Al_2O_3 destruction occurred as following:

$$Al_2O_3 + 6Cl^{-} \rightarrow 2AlCl_3 + 3O^{2-} \quad (21)$$

$$Al^{3+} + 3OH^{-} \rightarrow Al(OH)_3 \quad (22)$$

Thereby, it was concluded that the adsorbed CM-film isolated the chloride attack and also increased the process of corrosion reactions. Together with the surficial Al_2O_3, coumarin significantly inhibited the corrosion-induced pinholes on the aluminum surface.

Furthermore, coumarin concentration displayed a remarkable influence on inhibition effect. As aforementioned, both the molecular dynamics simulation and experiment determined that there was an optimal value of coumarin contents, lower or higher than this value would reduce the corrosion inhibition effect. Herein, there were three main scenarios, as shown in Fig. 11. (I) When coumarin concentration was below the optimal value, CM-film cannot provide continuous coverage on the aluminum surface for insufficient coumarin concentration, thus missing the complete protection on metal matrix. Whereas, (II) the excess concentration would also decrease the corrosion protection. Molecular dynamics simulation has demonstrated that the excess inhibitors induced a messy arrangement of molecules. Such negative effect was related to the competitive adsorption of molecule on metallic surface, which was frequency observed in the fields of molecular adsorption, as depicted in literatures.[53–56] The excess molecules resulted in competitive and unstable adsorption, signifying antagonistic effects between coumarin molecules and then deteriorating the anti-corrosion propensity of adsorption film.[55]

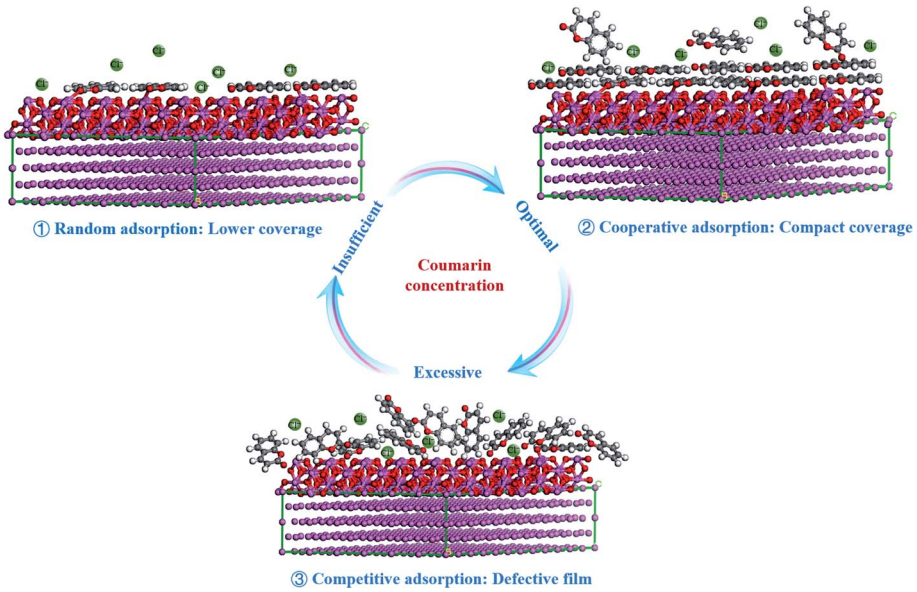

Fig. 11 Effect of coumarin concentration on inhibition efficiency. There were three cases that resulted in a random, cooperative and competitive adsorption of coumarin on the aluminum surface, respectively.

Open Access Article. Published on 16 July 2021. Downloaded on 2/8/2026 1:31:28 PM.
This article is licensed under a Creative Commons Attribution-NonCommercial 3.0 Unported Licence.

(III) There was an optimal concentration of 0.5 wt%, at which cooperative adsorption effects occurred, leading to a more compact adsorption film and better protection.[56] Ultimately, coumarin completely isolated the exposed area necessary for aluminum dissolution and hydrogen evolution, thus enhancing the surficial corrosion resistance. Moreover, the inhibition efficiency is not impressive as expected on such a high concentration, which is distinguished with the reported inhibitors. The reason for this observation should be ascribed to the structure of coumarin. When compared to the reported inhibitors, such as thiazole derivatives, coumarin derivatives and other heterocyclic compounds, coumarin with a small molecular volume exhibits a small steric hindrance, which weakens its ability to repel corrosive ions.[6,7,11,33] Thus, the inhibition efficiency of coumarin occurs in a high concentration.

5. Conclusions

This work presented an illustration on corrosion inhibition of coumarin as a green inhibitor for aluminum strips/foils through the theoretical and experimental methods. Analysis of surface morphology and surface chemistry was systematically performed. Some conclusions were summarized as follows:

(1) Coumarin exhibited a higher adsorption reactivity in the water phase than that in the gas phase, and C=O structure in coumarin was the most favorable site for adsorption occurring. Coumarin adsorbed spontaneously on aluminum surface in a parallel manner, where electrons donation occurred from the aluminum surface to the inhibitor.

(2) Coumarin decreased the aluminum dissolution by suppressing both the anodic and cathodic reactions, which showed a synergistic effect with surficial Al_2O_3. Besides, both the molecule dynamic simulation and experiments confirmed that there was an optimal concentration of coumarin. The excess inhibitors resulted in competitive and unstable adsorption, thus reducing the spatial coverage over the metal surface.

(3) Coumarin was a potential green inhibitor for aluminum, which could strongly confine the corrosion-induced pinholes on aluminum strips/foils, especially at the optimal concentration of 0.5 wt% with the maximum corrosion efficiency of 89.6%. Both the insufficient and excess concentrations of coumarin would lead to a defective film. Ultimately, coumarin could be further exploited as a green inhibitor for industrial and engineering applications.

Author contributions

Huajie Tang: conceptualization, methodology, formal analysis, investigation, visualization writing – original draft, writing review & editing. Jianlin Sun: validation, supervision. Daoxin Su: analysis, writing – review & editing. Ying Huang: writing – review & editing. Ping Wu: writing –review & editing, validation.

Conflicts of interest

There are no conflicts to declare.

Acknowledgements

This work was supported by the Nation Natural Science Foundation of China (No. 51874036), Beijing Natural Science Foundation (No. 2182041) and Scientific research project of Beijing Municipal Commission of Education (KM201911417002). The author also thanks professor Junhong Chen for his software support in the calculation section.

References

1 O. Taeri, A. Hassanzadeh and R. Fateme, *ChemElectroChem*, 2020, **7**, 2123–2135, DOI: 10.1002/celc.202000211.
2 M. Mokhtar, M. Z. M. Talib, E. H. Majlan, S. M. Tasirin, W. M. F. W. Ramli, W. R. W. Daud and J. Sahari, *J. Ind. Eng. Chem.*, 2015, **32**, 1–20, DOI: 10.1016/j.jiec.2015.08.004.
3 D. P. Wang, L. X. Gao, D. Q. Zhang, D. Yang, H. X. Wang and T. Lin, *Mater. Chem. Phys.*, 2016, **169**, 142–151, DOI: 10.1016/j.matchemphys.2015.11.041.
4 C. Lu, S. L. Mu, J. Du, K. Zhang, M. C. Guo and L. Chen, *RSC Adv.*, 2020, **10**, 36654–36666, DOI: 10.1039/d0ra07201j.
5 P. Yu, Z. X. Lian, J. K. Xu and H. D. Yu, *RSC Adv.*, 2021, **11**, 847–855, DOI: 10.1039/d0ra08674f.
6 M. Gobara, A. Baraka and R. Akid, *RSC Adv.*, 2020, **10**, 2227–2240, DOI: 10.1039/c9ra09552g.
7 D. Mahalakshmi, V. Hemapriya, E. Subramaniam and S. Chitra, *J. Mol. Liq.*, 2019, **284**, 316–327, DOI: 10.1016/j.molliq.2019.03.158.
8 D. K. Verma, S. Kaya and E. Ech-chihbi, *J. Mol. Liq.*, 2021, **329**, 115531, DOI: 10.1016/j.molliq.2021.115531.
9 H. J. Tang, J. L. Sun, Z. L. Zhao and J. Q. He, *Surf. Topogr.: Metrol. Prop.*, 2020, **8**, 025034, DOI: 10.1088/2051-672X/ab9e44.
10 H. J. Tang, J. L. Sun, Z. L. Zhao and Z. Han, *Trans. ASME, J. Tribol.*, 2021, **143**, 021901, DOI: 10.1115/1.4047857.
11 S. Xiong, D. Liang, Z. X. Ba, Z. Zhang and S. Luo, *Appl. Surf. Sci.*, 2019, **492**, 399–406, DOI: 10.1016/j.apsusc.2019.06.253.
12 I. L. Lehr and S. B. Saidman, *Electrochim. Acta*, 2006, **51**, 3249–3255, DOI: 10.1016/j.electacta.2005.09.017.
13 S. John and A. Joseph, *Mater. Corros.*, 2013, **64**, 625–632, DOI: 10.1002/maco.201206782.
14 J. L. Gazquez, A. Cedillo and A. Vela, *J. Phys. Chem. A*, 2007, **111**, 1966–1970, DOI: 10.1021/jp065459f.
15 C. Verma, M. Quraishi, E. Ebenso, I. Obot and l. Assyry, *J. Mol. Liq.*, 2016, **219**, 647–660, DOI: 10.1016/j.molliq.2016.04.024.
16 B. Gomez, N. Likhanova, M. Dominguez-Aguilar, R. Martinez-Palou, A. Vela and J. L. Gazquez, *J. Phys. Chem. B*, 2006, **110**, 8928–8934, DOI: 10.1021/jp057143y.
17 G. K. Jayaprakash and R. Flores-Moreno, *Electrochim. Acta*, 2017, **248**, 225–231, DOI: 10.1016/j.electacta.2017.07.109.
18 G. K. Jayaprakash, B. E. K. Swamy, N. Casillas and R. Flores-Moreno, *Electrochim. Acta*, 2017, **258**, 1025–1034, DOI: 10.1016/j.electacta.2017.11.154.
19 R. R. Contreras, P. Fuentealba, M. Galvan and P. Perez, *Chem. Phys. Lett.*, 1999, **304**, 405–413, DOI: 10.1016/S0009-2614(99)00325-5.

© 2021 The Author(s). Published by the Royal Society of Chemistry

Open Access Article. Published on 16 July 2021. Downloaded on 2/8/2026 1:31:28 PM. This article is licensed under a Creative Commons Attribution-NonCommercial 3.0 Unported Licence.

20 H. Jafari, I. Danaee, H. Eskandari and M. RashvandAvei, *Ind. Eng. Chem. Res.*, 2013, **52**, 6617–6632, DOI: 10.1021/ie400066x.
21 Y. J. Qiang, L. Guo, S. T. Zhang, W. P. Li, S. S. Yu and J. H. Tan, *Sci. Rep.*, 2016, **6**, 33305, DOI: 10.1038/srep33305.
22 E. E. Oguzie, C. B. Adindu, C. K. Enenebeaku, C. E. Ogukwe, M. A. Chidiebere and K. L. Oguzie, *J. Phys. Chem. C*, 2012, **116**, 13603–13615, DOI: 10.1021/jp300791s.
23 R. Solmaz, *Corros. Sci.*, 2014, **81**, 75–84, DOI: 10.1016/j.corsci.2013.12.006.
24 J. J. Fu, H. S. Zang, Y. Wang, S. N. Li, T. Chen and X. D. Liu, *Ind. Eng. Chem. Res.*, 2012, **51**, 6377–6386, DOI: 10.1021/ie202832e.
25 S. M. Hiremath, A. S. Patil, C. S. Hiremath, M. Basangouda, S. S. Khemalapure, N. R. Patil, S. B. Radder, S. J. Armakovic and S. Armakovic, *J. Mol. Struct.*, 2018, **1178**, 1–17, DOI: 10.1016/j.molstruc.2018.10.007.
26 N. U. Inbaraj and G. V. Prabhu, *Prog. Org. Coat.*, 2018, **115**, 27–40, DOI: 10.1016/j.porgcoat.2017.11.007.
27 M. Mobin, S. Zehra and R. Aslam, *RSC Adv.*, 2016, **6**, 5890–5902, DOI: 10.1039/C5RA24630J.
28 T. Wilberforce, O. Ijaodola, E. Ogungbemi, F. N. Khatib, T. Leslie, Z. El-Hassan, J. Thomposon and A. G. Olabi, *Renewable Sustainable Energy Rev.*, 2019, **113**, 109286, DOI: 10.1016/j.rser.2019.109286.
29 H. M. Jia, X. H. Feng and Y. S. Yang, *J. Mater. Sci. Technol.*, 2017, **34**, 1229–1235, DOI: 10.1016/j.jmst.2017.06.009.
30 X. H. Liu, L. L. Liu, F. L. Sui, H. Y. Bi, E. Chang and M. C. Li, *J. Solid State Electrochem.*, 2020, **24**, 1197–1206, DOI: 10.1007/s10008-020-04614-1.
31 A. Pardo, M. C. Merino, A. E. Coy, F. Viejo, R. Arrabal and E. Matykina, *Corros. Sci.*, 2008, **50**, 1796–1806, DOI: 10.1016/j.corsci.2008.04.005.
32 Y. Yang, H. T. Zeng, S. S. Xin, X. L. Hou and M. C. Li, *Corros. Sci.*, 2020, **165**, 108383, DOI: 10.1016/j.corsci.2019.108383.
33 H. J. Tang, J. L. Sun, X. D. Yan and P. Wu, *RSC Adv.*, 2019, **9**, 34617–34626, DOI: 10.1039/c9ra05740d.
34 R. H. Cao, L. N. Xu, B. L. Jiang, M. J. Gao, D. R. Qu, G. B. Shan, S. J. Xu and L. J. Qiao, *Corros. Sci.*, 2019, **164**, 108339, DOI: 10.1016/j.corsci.2019.108339.
35 R. Sanchez-Tovar, M. T. Montanes and J. Garcia-Anton, *Corros. Sci.*, 2012, **60**, 118–128, DOI: 10.1016/j.corsci.2012.04.001.
36 K. Feng, Z. G. Li, X. Cai and P. K. Chu, *Surf. Coat. Technol.*, 2010, **205**, 85–91, DOI: 10.1016/j.surfcoat.2010.06.009.
37 T. Bellezze, G. Giuliani, A. Vicere and G. Roventi, *Corros. Sci.*, 2018, **130**, 12–21, DOI: 10.1016/j.corsci.2017.10.010.
38 S. V. Lamaka, M. L. Zheludkevich, K. A. Yasakau, M. F. Montemor and M. G. S. Ferreira, *Electrochim. Acta*, 2007, **52**, 7231–7247, DOI: 10.1016/j.electacta.2007.05.058.
39 L. C. Hu, S. T. Zhang, W. H. Li and B. R. Hou, *Corros. Sci.*, 2010, **52**, 2891–2896, DOI: 10.1016/j.corsci.2010.04.038.
40 D. Snihirova, S. V. Lamaka, M. M. Cardoso, J. A. D. Condeco, H. E. C. S. Ferreira and M. de Fatima Montemor, *Electrochim. Acta*, 2014, **145**, 123–131, DOI: 10.1016/j.electacta.2014.09.009.
41 K. F. Khaled and N. Hackerman, *Mater. Chem. Phys.*, 2003, **82**, 949–960, DOI: 10.1016/j.matchemphys.2003.08.007.
42 K. Xhanari and M. Finsgar, *Arabian J. Chem.*, 2016, **12**, 4646–4663, DOI: 10.1016/j.arabjc.2016.08.009.
43 H. J. Tang, J. L. Sun, J. Q. He and P. Wu, *J. Ind. Eng. Chem.*, 2020, **94**, 105–121, DOI: 10.1016/j.jiec.2020.12.020.
44 M. A. Amin, E. M. Ahmed, N. Y. Mostafa, M. M. Alotibi, G. Darabdhara, M. R. Das, J. Wysocka, J. Ryl and S. Abd Ei Rehim, *ACS Appl. Mater. Interfaces*, 2016, **8**, 23665, DOI: 10.1021/acsami.6b05630.
45 A. M. Abdel-Gaber, E. Khamis, H. Abo-Eldahab and S. H. Adeel, *Mater. Chem. Phys.*, 2010, **124**, 773–779, DOI: 10.1016/j.matchemphys.2010.07.059.
46 B. Wang, L. W. Zhang, Y. Su, Y. Xiao and J. Liu, *Acta Metall. Sin.*, 2013, **26**, 581–587, DOI: 10.1007/s40195-013-0018-y.
47 B. Zhang, J. Wang, B. Wu, X. W. Guo, Y. J. Wang, D. Chen, Y. C. Zhang, K. Du, E. E. Oguzie and X. L. Ma, *Nat. Commun.*, 2018, **9**, 2559, DOI: 10.1038/s41467-018-04942-x.
48 G. Moretti, F. Guidi and F. Fabris, *Corros. Sci.*, 2013, **76**, 206–218, DOI: 10.1016/j.corsci.2013.06.044.
49 L. Garrigues, N. Pebere and F. Dabosi, *Electrochim. Acta*, 1996, **41**, 1209–1215, DOI: 10.1016/0013-4686(95)00472-6.
50 M. A. Amin, S. S. A. El-Rehim, E. E. F. El-Sherbini, O. A. Hazzazi and M. N. Abbas, *Corros. Sci.*, 2009, **51**, 658–667, DOI: 10.1016/j.corsci.2008.12.008.
51 S. I. Pyun and S. M. Moon, *J. Solid State Electrochem.*, 2000, **4**, 267–272, DOI: 10.1007/s100080050203.
52 S. M. Moon and S. I. Pyun, *Electrochim. Acta*, 1999, **44**, 2445–2454, DOI: 10.1016/s0013-4686(98)00368-5.
53 Z. P. Li, X. F. Li, Y. W. Zhang, T. H. Ren, Y. D. Zhao, X. Q. Zeng and E. Van der Heide, *Appl. Surf. Sci.*, 2014, **308**, 91–99, DOI: 10.1016/j.apsusc.2014.04.116.
54 J. Zhao, H. Duan and R. Jiang, *Corros. Sci.*, 2015, **91**, 108–119, DOI: 10.1016/j.corsci.2014.11.007.
55 M. M. Solomon, S. A. Umoren, I. B. Obot, A. A. Sorour and H. Gerengi, *ACS Appl. Mater. Interfaces*, 2018, **10**, 28112–28129, DOI: 10.1021/acsami.8b09487.
56 A. Y. Musa, A. B. Mohamad, A. A. H. Kadhum, M. S. Takriff and L. T. Tien, *Corros. Sci.*, 2011, **53**, 3672–3677, DOI: 10.1016/j.corsci.2011.07.010.

© 2021 The Author(s). Published by the Royal Society of Chemistry